THE JOURNAL OF PHYSICAL CHEMISTRY B
A JOURNAL OF THE AMERICAN CHEMICAL SOCIETY

pubs.acs.org/JPCB

Article

Effective Na^+-Binding Ability and Molecular Assembly of an Alkylamide-Substituted Penta(ethylene)glycol Derivative

Shinya Seto, Takashi Takeda, Norihisa Hoshino, and Tomoyuki Akutagawa*

Cite This: *J. Phys. Chem. B* 2021, 125, 6349–6358

Read Online

ACCESS | Metrics & More | Article Recommendations | Supporting Information

ABSTRACT: A new amphiphilic penta(ethylene glycol) derivative (**1**) bearing two hydrogen-bonding $-CONHC_{14}H_{29}$ chains was prepared. Compound **1** exhibited ion-recognition abilities for Na^+ and K^+, and its properties were compared with those of the macrocyclic [18]crown-6. Although both compound **1** and [18]crown-6 have six ether oxygen atoms ($-OC_2H_2-$), the Na^+-binding ability of the former was much higher than that of the latter. K^+-binding ability of cyclic [18]crown-6 was much higher than its Na^+-binding ability, while the reverse was true for acyclic compound **1**. Single-crystal X-ray structural analysis of Na^+·**1**·$B(Ph)_4^-$·$(hexane)_2$ at 100 K revealed the existence of a wrapped Na^+-coordination by six ether and one carbonyl oxygen atoms of **1**, which was further stabilized by intramolecular N−H···O═ hydrogen-bonding interactions. The complex phase transition during glass (G) formation and recrystallization was confirmed in the thermal cycle of Na^+·**1**·$B(Ph)_4^-$, whose molten state showed two kinds of liquid phases, Na^+-complexed (Na^+·**1**) + $B(Ph)_4^-$ and completely dissociated Na^+ + **1** + $B(Ph)_4^-$. The Na^+ conductivity of the molten state was 2 orders of magnitude higher than that of the G phase.

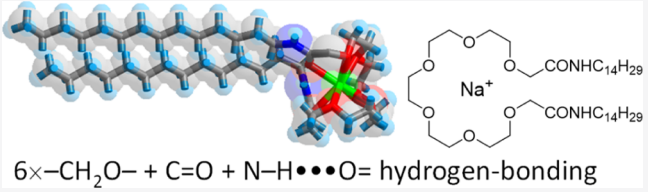

1. INTRODUCTION

Crown ether derivatives can recognize a variety of cations based on the size of the central cavity of macrocycles.[1−4] For instance, Na^+ and K^+ cations can fit well into the cavities of [15]crown-5 and [18]crown-6, respectively, forming planar cyclic Na^+([15]crown-5) and K^+([18]crown-6) structures.[4−6] The driving force for binding cations (M^+) inside the cavity of a crown ether is the electrostatic attractive interaction of the lone pairs of oxygen atoms of the macrocyclic ether. Additionally, the oxygen atoms have a much higher affinity for hard cations than soft cations.[1−3,7,8] Based on the complex formation constant (pK), the affinity of [18]crown-6 for alkali-metal ions in the CH_3CN solution phase decreases in the order K^+ (pK = 5.46) > Rb^+ (pK = 4.89) ∼ Cs^+ (pK = 4.83) > Na^+ (pK = 4.21), depending on the compatibility between the cavity size and ionic radii.[9,10] For instance, owing to the much smaller pore diameter of [15]crown-5 compared to that of [18]crown-6, the affinity of Na^+ ions was much higher than that for K^+ one. The pK values of [15]crown-5 for Na^+ and K^+ cations are 5.38 and 3.98, respectively, while those of [18]crown-6 for the same cations are 4.21 and 5.46, respectively, in CH_3CN.[9,10] Therefore, the strategic design of the macrocyclic ring size is an important factor for controlling the cation selectivity. Similar electrostatic interactions at the oxygen atoms of the ether units ($-OC_2H_4-$) for M^+ have been reported in an acyclic oligo(ethylene glycol) derivative.[11−13] These acyclic ethers can also recognize alkali-metal ions, and the pK values of dimethyl-penta(ethylene glycol); pentaglyme, for Na^+ and K^+ cations are 1.52 and 2.20, respectively,[14] while those of [18]crown-6 for the same cations are 4.36 and 6.06, respectively, in CH_3OH.[9,10] Therefore, the pK value of the macrocyclic system is 3 or 4 orders of magnitude higher than that of the acyclic system.[14] The conformational freedom of acyclic oligo(ethylene glycol) derivatives drastically decreases the M^+-binding ability relative to the binding ability of conformationally rigid cyclic crown ethers. This is known as the macrocyclic effect.[15,16]

The ion-recognized crown ether and oligo(ethylene glycol) derivatives can form interesting ion-encapsulated static and dynamic molecular assemblies.[17−24] For instance, a regular array of crown ethers forms an artificial ionic channel that has been applied for the design of functional ion-transport systems in molecular assemblies.[25−27] The ionic channels of M^+([18]-crown-6), where M^+ = Li^+, Na^+, and Cs^+, have been introduced into the electrically conducting [Ni(dmit)$_2$] salts ($dmit^{2-}$ = 2-thioxo-1,3-dithiole-4,5-dithiolate); the ion dynamics inside the channels have been investigated based on the electrical conductivity and magnetic susceptibility.[28−30] A small-sized Li^+ cation inside the cavity of [18]crown-6 has motional freedom, while the dynamics of a Na^+ cation inside [18]crown-6 is subtly restricted due to the effective binding of Na^+ to the six ether oxygen atoms. In addition, the large-sized Cs^+ cation

Received: April 8, 2021
Revised: May 20, 2021
Published: June 4, 2021

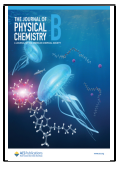

https://doi.org/10.1021/acs.jpcb.1c03188
J. Phys. Chem. B 2021, 125, 6349–6358

Scheme 1. Molecular Structures of 1 and the Na^+·1 Complex with the $B(Ph)_4^-$ Counter Anion

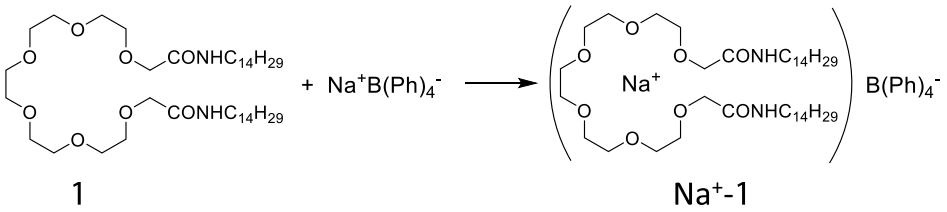

cannot pass through the cavity of [18]crown-6 and is fixed between the [18]crown-6 molecules. Such cation dynamics and its arrangement in the crystal lattice affect the electrical conducting behavior of the regular π-stack of $[Ni(dmit)_2]$ via the generation of periodic and random potentials for the conduction electrons.[28,29] The cation structure of K^+[penta(ethylene glycol)] has been introduced into the electrically conducting $[Ni(dmit)_2]$ crystals.[31] However, the low M^+-binding ability of oligo(ethylene glycol) derivatives restricts the crystal formation of the $[Ni(dmit)_2]$ salt, including a variety of supramolecular cations. In contrast, Li^+-conducting materials such as Li^+-coordination polymers of poly(ethylene glycol) derivatives have been extensively developed for their application as electrolytes in Li^+ secondary batteries.[32,33] Structural analysis of the Li^+[poly(ethylene glycol)] derivative revealed a helical Li^+-coordination between the Li^+ cation and ether oxygen atoms.

Oligo(ethylene glycol) and poly(ethylene glycol) derivatives have been widely utilized for the formation of specific molecular assemblies such as micelles and vesicles.[34,35] Highly water soluble ethylene glycol chains are useful for designing drug delivery systems and for fabricating biocompatible molecular systems.[36,37] On the other hand, molecular assemblies of hydrophobic molecules bearing long alkyl chains are stabilized by multiple van der Waals interactions; these molecular assemblies include micelles, vesicles, and Langmuir–Blodgett films.[38−40] Although van der Waals interactions are much weaker than electrostatic, hydrogen-bonding, and charge-transfer interactions, the multitude of such interactions in long alkyl chain compounds effectively enhances the total energy of the intermolecular interactions. The intermolecular van der Waals interaction between the alkyl chains is more than that between the oligo(ethylene glycol) chains, which was confirmed by the considerably higher melting point of *n*-alkanes than that of the oligo(ethylene glycol) derivatives with the same chain length.[41,42] For instance, the melting point of the pentadecane (n-$C_{15}H_{32}$) crystal (283 K) was 40 K higher than that of the tetraglyme of $C_{10}H_{22}O_5$ (243 K).[41] A useful crystal engineering approach to enhance the intermolecular interaction has been demonstrated by utilizing the molecular fastener effect in electrically conducting tetrathiafulvalene (TTF) derivatives bearing four long alkylthio chains ($-SC_nH_{2n+1}$), where the multiple van der Waals interactions between the alkylthio-chains effectively bind the TTF π-molecular system in a one-dimensional (1D) column.[42,43] The conformational freedom of the alkyl chain can be partially melted even in solids. For instance, several *n*-alkane crystals showed an ordered crystal–plastic crystal phase transition by thermally activated 1D rotation along the long axis of the molecule.[44,45] In addition, most of the thermotropic liquid crystalline molecules have both a rigid core and flexible lateral alkyl chain(s), and the transition to the liquid crystal phase was accompanied by the melting of the alkyl chain(s) and the free rotation of the rigid core along the long axis of the molecule.[46,47] Thermal conversion between the trans and gauche conformation of the alkyl chain occurs typically in liquid phases, and such dynamics play an important role in the appearance of the liquid crystal phase. In liquid crystalline materials, alkyl chains such as $-C_nH_{2n+1}$, $-OC_nH_{2n+1}$, $-COOC_nH_{2n+1}$, and $-OOCC_nH_{2n+1}$ are fused at the rod-like rigid core. Among them, the alkylamide group of $-CONHC_nH_{2n+1}$ is an interesting hydrogen-bonding structural unit for stabilizing the liquid crystal phase, as first demonstrated by Matsunaga et al. for the discotic hexagonal columnar (Col_h) liquid crystal phase.[48−50] The effective intermolecular N–H···O= hydrogen-bonding interaction enhances the order of molecular assembly in the intrinsic liquid state, leading to the appearance of the mesophase before melting to the liquid phase. For instance, a benzene derivative bearing three $-CONHC_nH_{2n+1}$ chains at the 1, 3, and 5-positions (3BC) forms the Col_h liquid crystal phase by the aid of intermolecular N–H···O= hydrogen-bonding interactions.[49,50] Interestingly, the application of electric field (E) along the hydrogen-bonding column of 3BC resulted in a ferroelectric response in the polarization–electric field (P–E) curve, wherein the dipole moment of each hydrogen-bonding chain was inverted by the application of outer E along the π-stack.[51−55] Further chemical design of the central core, from simple benzene to functional π-molecular systems such as pyrene and tetrabenzoporphyrin, has been utilized for fabricating multifunctional molecular materials.[56−59] For instance, a pyrene derivative bearing four $-CONHC_{14}H_{29}$ chains exhibits ferroelectricity, fluorescence, and current-switching behavior. Most importantly, it can form multifunctional molecular assemblies such as organogels and nanofibers[56−58] The non π-planar 2,5-dimethylhelicene derivative bearing two $-CONHC_{14}H_{29}$ chains also exhibited ferroelectricity, as evident from the P–E hysteresis curve. Moreover, single-crystal X-ray structural analysis of this molecular system revealed the presence of a two-dimensional (2D) N–H···O= hydrogen-bonding network.[60] The polar alkylamide chain is one of the useful structural units to design dynamic molecular assemblies.

In this study, we designed a penta(ethylene glycol) derivative (**1**), which exhibited ion-recognition ability and contained hydrogen-bonding N–H···O= sites and hydrophobic long alkyl chains of $-CONHC_{14}H_{29}$ (Scheme 1). It was further applied as a new hydrogen-bonding ion-recognition molecular system. The six ether oxygen atoms of the penta(ethylene glycol) unit in **1** could adopt a cyclic conformation by coordinating to an alkali metal ion. The coexistence of a hydrophilic cation-binding M^+[penta(ethylene glycol)] unit and the hydrophobic long $-C_{14}H_{29}$ alkyl chains renders the ion-recognized M^+·**1** complex amphiphilic. Owing to the cation-binding ability of acyclic compound **1**, together with the N–H···O= hydrogen-bonding interaction, the

https://doi.org/10.1021/acs.jpcb.1c03188
J. Phys. Chem. B 2021, 125, 6349−6358

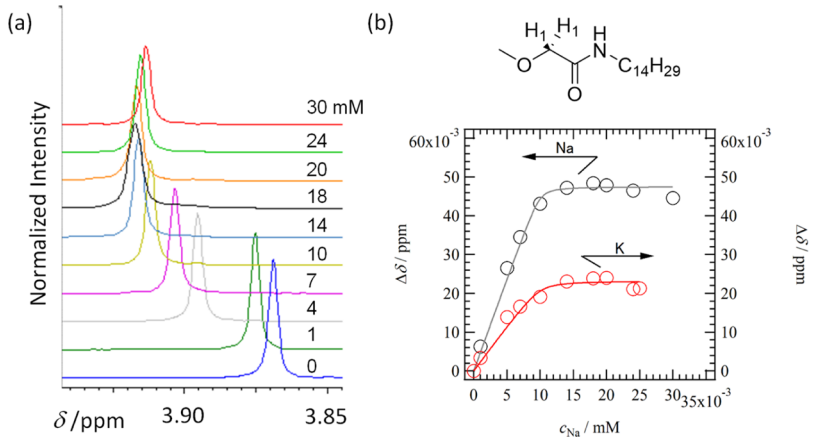

Figure 1. Na^+- and K^+-binding abilities of **1** in $CDCl_3$−CD_3CN (v/v = 1/9). (a) Na^+ concentration (c_{Na})-dependent change in δ-values of the C−H_1 proton of **1** (at a fixed concentration of 10 mM) upon the addition of $Na^+{\cdot}BPh_4^-$. (b) c_{Na}- and c_K-dependent changes in $\Delta\delta$ values of **1** upon the addition of $Na^+{\cdot}BPh_4^-$ (left scale) and $K^+{\cdot}BPh_4^-$ (right scale).

molecular conformation changes drastically after M^+ recognition and provides higher conformational freedom than that in cyclic [18]crown-6. The Na^+- and K^+-binding abilities of acyclic molecule **1** in the solution phase were compared with those of cyclic [18]crown-6. The molecular assemblies of **1** and the $Na^+{\cdot}$**1** complex were examined in terms of their thermal stability, phase transition behavior, molecular structure, packing structure, dielectric response, and ionic conductivity. This is expected to provide further design strategies for functional molecular assemblies based on hydrogen-bonding acyclic ion-recognition molecules.

2. METHODS

2.1. Physical Measurements. ^1H NMR spectra were recorded on a Bruker AVANCE III 400 NMR spectrometer, and chemical shifts (δ, ppm) were obtained relative to tetramethylsilane as an internal standard. Temperature-dependent infrared (IR) spectra were recorded in the range 400−4000 cm^{-1} using KBr pellets on a Thermo Fisher Scientific Nicolet 6700 spectrophotometer with a resolution of 4 cm^{-1}. Thermogravimetric (TG) analysis and differential scanning calorimetry (DSC) were conducted using a Rigaku Thermo plus TG8120 thermal analysis station and Mettler DSC1-T with an Al_2O_3 reference, respectively, with a heating and cooling rate of 5 K min^{-1} under a nitrogen atmosphere. The temperature-dependent dielectric constants were measured using the two-probe AC impedance method from 100 Hz to 1 MHz (Hewlett-Packard, HP4194A); a Linkam LTS-E350 temperature controller system was used for the measurement. Compound **1** or $Na^+{\cdot}$**1** was fabricated in its liquid state into an indium tin oxide (ITO) glass (SZ-A311P6N) and was sandwiched by the corresponding ITO glass to form the dielectric measurement cell with an average electrode gap of 2 μm. Temperature-dependent powder X-ray diffraction (PXRD) was performed using a Rigaku SmartLab diffractometer with Cu Kα (λ = 1.54187 Å) radiation.

2.2. Preparation of 1. *2.2.1. Preparation of Di-tert-butyl 3,6,9,12,15,18-Hexaoxaicosane-1,20-dioate (**1a**).* Aq. NaOH (50 wt %, 50 mL) was poured into a solution of pentaethylene glycol (5.07 g, 21.3 mmol) in toluene (50 mL) at 273 K. After the addition of tetrabutylammonium hydrogen sulfate (16.0 g, 46.8 mmol) and *tert*-butyl bromoacetate (12.4 mL, 85.1 mmol), the reaction mixture was stirred at 273 K for 10 min and further stirred at 298 K for 30 min. After quenching the reaction by the addition of water, the solution was washed with saturated NH_4Cl, $NaHCO_3$, and brine (30 mL × 1) and dried on sodium sulfate overnight. The solvent was removed in vacuum, and the crude product (9.15 g) was purified by silica gel column chromatography (ethyl acetate/toluene/ethanol = 10/10/1) to afford colorless oil compound **1a** (3.66 g 7.84 mmol) with a yield of 37%. ^1H NMR: δ 4.02 (s, 4H), δ 3.70 (m, 20H), δ 1.48 (s, 18H).

*2.2.2. Preparation of 3,6,9,12,15,18-Hexaoxaicosane-1,20-dioic Acid (**1b**).* Trifluoroacetic acid (12.4 mL) was slowly added to a solution of **1a** (3.66 g 7.84 mmol) in CH_2Cl_2 (10 mL) and stirred at 298 K for 2 h. The solvent and an excess amount of trifluoroacetic acid were removed in vacuum. Compound **1b** (6.36 g) was used for the next reaction without purification.

*2.2.3. N^1,N^{20}-Ditetradecyl-3,6,9,12,15,18-hexaoxaicosanediamide (**1**).* Compound **1b** (6.36 g, 18.0 mmol) in $SOCl_2$ (31.5 mL) was stirred overnight at 338 K, and the residual $SOCl_2$ was removed in vacuum. The reaction products were dissolved in anhydrous CH_2Cl_2 (30 mL), and triethylamine (7.5 mL, 53.8 mmol) and tetradecylamine (9.59 g, 45.0 mmol) were added to the solution and stirred at 298 K for 5 days. After the addition of water, the organic layer was washed three times with saturated brine and dried overnight on sodium sulfate. After removing CH_2Cl_2, the crude product was purified by silica gel column chromatography (eluted using toluene/ethanol in the ratio 8:2, 7:3, to 2:3) passing through activated carbon. The product was recrystallized from CH_3CN as a white powder (compound **1**, 1.47 g) with a yield of 9%. Elemental analysis: Calcd. for $C_{42}H_{84}N_2O_8$: C: 67.70, H: 11.36, N: 3.76. Found: C: 67.77, H: 11.61, N: 3.78. ^1H NMR (400 MHz, $CDCl_3$): δ 6.95 (s, 2H), 3.98 (s, 4H), 3.68−3.65 (m, 20H), 3.27 (q, J = 6.8 Hz, 4H), 1.52 (t, J = 6.8 Hz, 4H), 1.30−1.25 (m, 46H), 0.88 (t, J = 6.8 Hz, 6H).

2.3. Crystal Structure Determination. Single crystals of $Na^+{\cdot}$**1**$\cdot B(Ph)_4^-{\cdot}(hexane)_2$ were obtained by slow evaporation from a propanol−hexane (1:2 (v/v)) mixture. Crystallographic data were collected on a Rigaku RAPID-II diffractometer equipped with a rotating anode fitted with multilayer confocal optics, using Cu Kα (λ = 1.54187 Å) radiation from a graphite monochromator. Structural refinements were performed using the full-matrix least-squares method on F^2. Calculations were

https://doi.org/10.1021/acs.jpcb.1c03188
J. Phys. Chem. B 2021, 125, 6349−6358

performed using the crystal structure software packages. All the parameters, except for those of the hydrogen atoms, were refined using anisotropic temperature factors.[61,62] Crystal data of Na^+-**1**, $C_{78}H_{130}BN_2NaO_8$: F.W. = 1257.69, crystal dimensions, 0.30 × 0.05 × 0.01 mm^3, T = 100 K, triclinic $P\bar{1}$ (#2), a = 9.9634(5), b = 12.9623(6), c = 29.9897(15) Å, α = 96.640(7), β = 92.811(7), γ = 96.951(7)°, V = 3811.1(3) $Å^3$, Z = 2, D_{calcd} = 1.096 g cm^{-3}, μ = 5.807 cm^{-1}, 9285 collected, 7350 unique, R_{init} = 0.0510, R_1 = 0.0832, R_{all} = 0.1559, R_w = 0.2878, and G.O.F = 0.944. The maximum and minimum peaks on the final difference Fourier map corresponded to +0.36e^- and −0.32e^- $Å^{-3}$, respectively. CCDC-2076312.

3. RESULTS AND DISCUSSION

3.1. Ion Recognition Ability of Compound 1 in Solution. The pore radius of the central cavity of [18]-crown-6 (1.31 Å) is similar to the ion radius (r_i) of K^+ (1.38 Å), indicating a high K^+-binding ability with a pK of 5.46 in CD_3CN.[7] The pore size of [18]crown-6 is slightly larger than r_i of Na^+ (0.95 Å), and binding to Na^+ decreases the pK value by one order of magnitude (pK = 4.21) for the K^+-binding ability. The ion-recognition ability of oligo(ethylene glycol) is 3 or 4 orders of magnitude lower than that of a crown ether of a similar size.[7,8] However, conformational freedom of the acyclic molecular structure of the oligo(ethylene glycol) derivative depends on the ions. Figure 1a summarizes the change in chemical shift (δ, ppm) of the C−H_1 proton of **1** (at a fixed concentration of 10 mM) in $CDCl_3$−CD_3CN (v/v = 1/9) upon the addition of $Na^+{\cdot}BPh_4^-$ at a Na^+ concentration (c_{Na}) of up to 30 mM. The C−H_1 proton signals of **1** were shifted downfield from 3.87 ppm (c_{Na} = 0 mM) to 3.91 ppm (c_{Na} = 30 mM) upon the addition of Na^+ ions (Figure S2). Similar downfield shifts of the C−H_1 proton of **1** were observed upon the addition of $K^+{\cdot}BPh_4^-$, suggesting the K^+-binding ability in $CDCl_3$−CD_3CN (v/v = 1/9) (Figure S3). Figure 1b shows the ion (M = Na and K) concentration (c_M)-dependent shift of the δ value ($\Delta\delta$, ppm) of **1** upon the addition of Na^+ and K^+ ions. The $\Delta\delta$ values were saturated at high c_M for both Na^+ and K^+ ions, which was consistent with the first-order binding of **1** with M^+, that is, **1** + M^+ = $M^+{\cdot}$**1**, in the solution phase. The pK values of **1** for Na^+ and K^+ were found to be 4.30 and 3.89, respectively, upon curve fitting (Figure 1a). Interestingly, the pK value for Na^+ was higher than that for K^+. Although both [18]crown-6 and the penta(ethylene glycol) unit of **1** have six −OC_2H_4− oxygen atoms, the Na^+-binding ability of the acyclic compound **1** was much higher than that of [18]crown-6. The pK values of pentaglyme for Na^+ and K^+ were 1.52 and 2.20, respectively,[14] while those of [18]crown-6 for the same cations were 4.36 and 6.06, respectively, in CH_3OH.[9,10] Therefore, the Na^+-binding ability of acyclic compound **1** should be much higher than that of pentaglyme bearing the same number of −C_2H_4O− units within the molecule.

3.2. Phase Transition Behavior. Thermal stability and phase transition behavior of **1** and $Na^+{\cdot}$**1**$\cdot B(Ph)_4^-$ were evaluated by TG and DSC. The single crystals of $Na^+{\cdot}$**1**$\cdot B(Ph)_4^-{\cdot}(hexane)_2$ included 2 mol of the crystallization solvent, hexane, which was rapidly removed at 298 K. Weight losses of **1** and $Na^+{\cdot}$**1**$\cdot B(Ph)_4^-$ were observed at 500 and 480 K, respectively, in the TG curves (Figure S4), suggesting the slightly higher thermal stability of **1** than the cation−anion $Na^+{\cdot}$**1**$\cdot B(Ph)_4^-$ salt. Figure 2a shows the DSC curves of **1** and $Na^+{\cdot}1{\cdot}B(Ph)_4^-$. Solid **1** underwent a phase transition in two steps—S1−S2 at 336 K and S2−L at 357 K—in the heating cycle up to 373 K (Figure S5). The transition enthalpy changes (ΔH) were 24.7 and 97.4 kJ mol^{-1}, respectively. However, the L−S2 and S2−S1 phase transitions were observed at 330 (ΔH = −101.5 kJ mol^{-1}) and 320 K (ΔH = −31.5 kJ mol^{-1}) in the cooling process. This supercooling phenomenon exhibited by **1** was consistent with a first-order phase transition behavior.

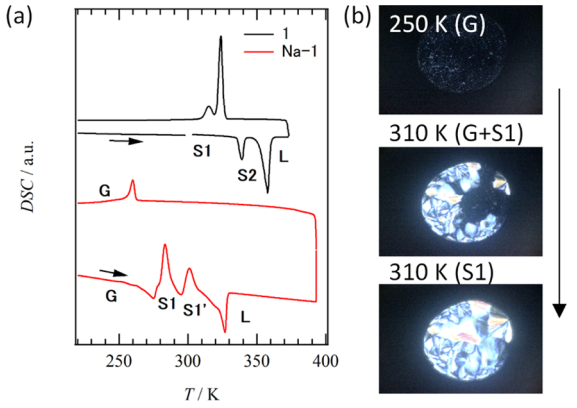

Figure 2. Phase transition behavior of solid **1** and $Na^+{\cdot}$**1**$\cdot B(Ph)_4^-$. (a) DSC curves of **1** (black) and $Na^+{\cdot}$**1**$\cdot B(Ph)_4^-$ (red), where S1, S1′, S2, G, and L represent solid 1, solid 1′, solid 2, glass, and isotopic liquid phases, respectively. (b) POM images of $Na^+{\cdot}$**1**$\cdot B(Ph)_4^-$ under cross-Nicole optical arrangements: the G phase at 250 K (top), the G + S1 phase at 310 K (middle), and the S1′ phase at 310 K (bottom).

A complex phase transition behavior was observed for the $Na^+{\cdot}$**1**$\cdot B(Ph)_4^-$ salt (red trace in Figure 2a). The melting point of $Na^+{\cdot}$**1**$\cdot B(Ph)_4^-$ was found to be 327 K, with ΔH = −78.1 kJ mol^{-1}, which was about ∼30 K lower than that of solid **1** (357 K). The POM images of the L phase were observed in a complete dark domain under a cross-Nicole optical arrangement and were consistent with the formation of an isotropic liquid state. The formation of a liquid crystal phase was not confirmed in the $Na^+{\cdot}$**1**$\cdot B(Ph)_4^-$ salt, while the viscous L phase suggested the existence of effective short-range electrostatic interactions. The formation of cation−anion pairs in the L phase corresponded to the ionic liquid state at 298 K in the cooling process, in the temperature range from 390 to 260 K. The supramolecular treatment of $Na^+{\cdot}B(Ph)_4^-$ by the addition of **1** formed the ionic liquid state, where the significant lowering of melting occurred to decrease the electrostatic interaction of Na^+. The birefringence POM image by crystallization was not recovered upon cooling the molten $Na^+{\cdot}$**1**$\cdot B(Ph)_4^-$ salt from the L phase at 390 K and a dark POM image was obtained (Figure S6). A small phase transition peak was observed at 260 K, with ΔH = 25.9 kJ mol^{-1}. No fluidic behavior was observed below 260 K and dark POM images were obtained. Therefore, the phase transition from L to glass (G) occurred in the $Na^+{\cdot}$**1**$\cdot B(Ph)_4^-$ molten salt via the supercooled state below 240 K. The stable G phase at 220 K was observed around 298 K in the second heating process, and two endothermic peaks were observed at 283 and 301 K corresponding to the crystallization of the G phase. The sum of the ΔH values for the G−S1 and G−S1′ phase transitions was 58.3 kJ mol^{-1}, which is slightly lower than the ΔH value at the melting point (−78.1 kJ mol^{-1}). After the first step, the G−S1 phase transition, both the G and S1 phases coexisted in the same domain as evident from the simultaneous appearance of the dark and bright domains in the POM image (Figure 2b, middle panel). The second step, S1−S1′ crystallization, resulted in the complete recovery of the bright crystalline

https://doi.org/10.1021/acs.jpcb.1c03188
J. Phys. Chem. B 2021, 125, 6349−6358

domain in the POM image (Figure 2b, lower panel). This thermal cycle of $Na^+\cdot\mathbf{1}\cdot B(Ph)_4^-$ was found to be reversible in the DSC measurements. The structural reconstruction of the cation−anion pair in the G phase is the origin of the G−S1 (S1′) phase transition of $Na^+\cdot\mathbf{1}\cdot B(Ph)_4^-$ during the heating process.

3.3. Structure of the Molecular Assembly. Structures of the molecular assemblies of **1** and $Na^+\cdot\mathbf{1}\cdot B(Ph)_4^-$ were investigated by temperature (T)-dependent XRD and single-crystal X-ray structural analyses, respectively. Single crystals of $Na^+\cdot\mathbf{1}\cdot B(Ph)_4^-\cdot(hexane)_2$ were successfully obtained by slow evaporation from a propanol−hexane mixture; the crystals were unstable in air at 298 K due to the rapid elimination of hexane molecules. Figure 3 summarizes the crystal structure of

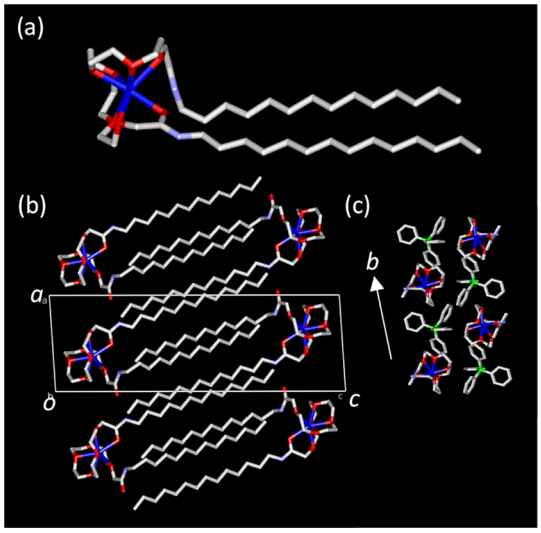

Figure 3. Crystal structure of $Na^+\cdot\mathbf{1}\cdot B(Ph)_4^-\cdot(hexane)_2$. (a) Molecular structure of $Na^+\cdot\mathbf{1}$. (b) Unit cell viewed along the b axis. The bulky $B(Ph)_4^-$ anion and hexane are omitted for clarity. (c) 2D cation−anion bilayer arrangement in the ab plane.

$Na^+\cdot\mathbf{1}\cdot B(Ph)_4^-\cdot(hexane)_2$ at 100 K (Figure S7). Structural information on the Na^+-coordination from **1** clarified the high Na^+-binding ability. Six ether oxygen atoms effectively interacted with Na^+, with the following $Na^+\cdots O$ distances (d_{Na-O}): d_{Na-O1} = 2.457(7), d_{Na-O2} = 2.393(6), d_{Na-O3} = 2.403(5), d_{Na-O4} = 2.394(6), d_{Na-O5} = 2.406(5), and d_{Na-O6} = 2.511(6) Å; the average $Na^+\cdots O$ distance was 2.42 Å. In addition, one carbonyl oxygen atom (O═) was coordinated to Na^+ with d_{Na-O} = 2.405(5) Å, resulting in a hepta-coordinated structure around Na^+. Furthermore, an additional N−H···O═ intramolecular hydrogen-bonding interaction with d_{N-H} = 3.061(7) Å stabilized the Na^+-binding cyclic molecular conformation (Figure S8). In the Na^+([18]crown-6)Br^- single crystal, the Na^+ ion existed inside the cavity of [18]crown-6 and was surrounded by six ether oxygen atoms with d_{Na-O1} = 2.464(3), d_{Na-O2} = 2.618, and d_{Na-O3} = 2.679 Å. The other three Na−O distances were longer than 2.8 Å, and only weak interactions were present between Na^+ and the oxygen atoms. The mean d_{Na-O} distance (2.79 Å) in the Na^+([18]crown-6)Br^- crystal was 0.35 Å longer than that in $Na^+\cdot\mathbf{1}$, in which d_{Na-O} = 2.42 Å. Therefore, Na^+ was strongly bound in the wrapped-coordination of **1** with the aid of additional interactions at the carbonyl O═ site and by the intramolecular N−H···O═ hydrogen-bonding interaction. These could be modulated to an appropriate coordination distance in order to increase the pK of **1**; this was in contrast to cyclic [18]crown-6. On the other hand, the lower K^+-binding ability of **1** compared to the Na^+-binding ability was consistent with the absence of any crystals of $K^+\cdot\mathbf{1}\cdot B(Ph)_4^-\cdot(hexane)_2$. The large K^+ ion suppressed the formation of intramolecular N−H···O═ hydrogen-bonding interaction and destabilized the formation of the wrapped $K^+\cdot\mathbf{1}$ complex. Two long $-C_{14}H_{29}$ chains of the $Na^+\cdot\mathbf{1}$ complex elongated along the same direction and interacted with each other through multiple van der Waals interactions to stabilize the Na^+-binding molecular structure.

Figure 3b shows the unit cell of $Na^+\cdot\mathbf{1}\cdot B(Ph)_4^-\cdot(hexane)_2$ viewed along the b axis; the $B(Ph)_4^-$ anions and hexane were omitted for clarity. A lamellar-type 2D molecular assembly structure was observed in the alternate arrangement of the cation−anion bilayer and hydrophobic alkyl layer along the c axis (Figure S9). The hydrophobic $-C_{14}H_{29}$ chains assembled with each other in the ab plane, and hexane molecules were required to form the closest packing structure. The $Na^+\cdot\mathbf{1}$ cation and the bulky $B(Ph)_4^-$ anion were alternatively arranged in the ab plane (Figure 3c), forming a bilayer-type electrostatic cation−anion Coulomb layer that was sandwiched by the hydrophobic alkyl layers. The layer periodicity along the c axis was 29.9897(15) Å at 100 K.

Figure 4a shows the PXRD patterns of the S1 and S2 phases of solid **1**. The structures of the crystalline molecular assemblies of **1** were confirmed by the appearance of sharp

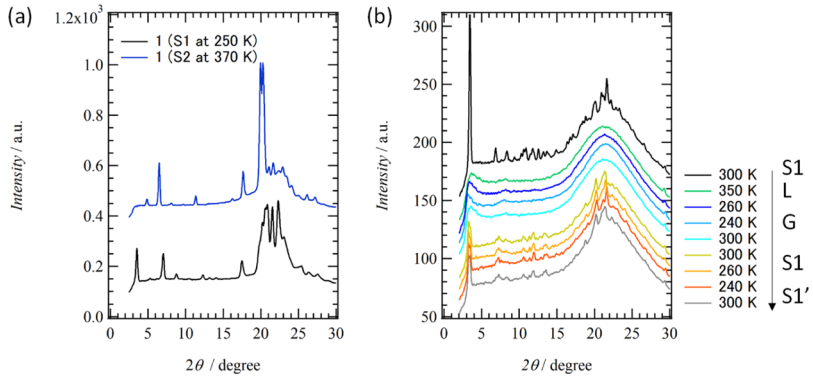

Figure 4. Structures of the molecular assemblies of **1** and $Na^+\cdot\mathbf{1}\cdot B(Ph)_4^-$. (a) PXRD patterns of solid **1** for the S1 phase (T = 250 K) and the S2 phase (T = 370 K). (b) T-dependent PXRD patterns of $Na^+\cdot\mathbf{1}\cdot B(Ph)_4^-$ from the initial S1 phase (T = 300 K), the L phase (T = 350 K), the G phase (T = 300, 260, and 240 K), and the S1−S1′ phases (T = 240, 260, and 300 K).

https://doi.org/10.1021/acs.jpcb.1c03188
J. Phys. Chem. B 2021, 125, 6349−6358

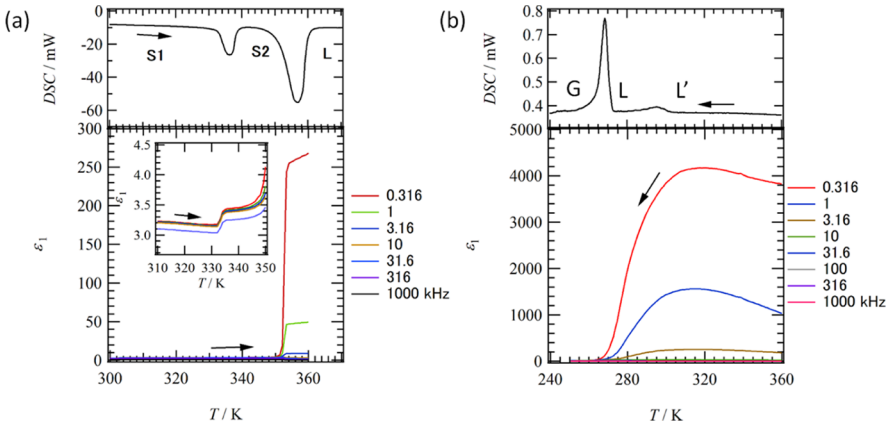

Figure 5. DSC curves and T- and f-dependent real components of the dielectric constants, ε_1, of (a) **1** in the heating process and (b) Na^+·**1**·$B(Ph)_4^-$ in the cooling process from 360 K.

Bragg reflections in the PXRD patterns of the S1 and S2 phases. An intense Bragg reflection peak was observed in the low-angle region at $2\theta = 6.512°$ in the S1 phase, corresponding to a d-spacing of 13.6 Å. For the S2 phase, peaks were observed at $2\theta = 3.520$ and 7.040°, corresponding to a d-spacing of 25.1 Å. The almost similar PXRD patterns of the S1 and S2 phases of solid **1** suggested a structure with nearly similar molecular assembly, along with a slight structural modulation at the S1−S2 phase transition. A broad diffraction peak at $2\theta \approx 20°$ overlapped with the sharp Bragg reflection peaks of the S1 and S2 phases, which was consistent with the partially melted state of the terminal $-C_{14}H_{29}$ chains.

The formation of the G phase was confirmed by the T-dependent PXRD patterns of Na^+·**1**·$B(Ph)_4^-$ (Figure 4b). The simulated PXRD pattern of Na^+·**1**·$B(Ph)_4^-$·$(hexane)_2$ based on the single-crystal X-ray structural analysis at 100 K indicated sharp Bragg reflection peaks and high crystallinity (Figure S10). However, removal of the crystallized hexane molecules at 298 K decreased the crystallinity, as evident from the appearance of a new broad hallow in the PXRD pattern of the initial S1 phase at 300 K (black curve in Figure 4b). Removal of hexane molecules from the space between the alkyl chain layer in the ab plane generated an empty crystalline space, where the motional freedom of the $-C_{14}H_{29}$ chains was thermally activated at 300 K. The broad reflection peak at $2\theta \approx 20°$ was consistent with the partially melted state of the alkyl chains in the S1 phase (T = 300 K). The sharp Bragg reflections completely disappeared upon the S1−L phase transition, and only a broad hallow was observed at $2\theta = 20°$. The same liquid-like PXRD patterns were maintained during the cooling of the L phase down to 240 K, which was consistent with the formation of the G phase. When the G phase was partially crystallized in the S1 phase in the second heating cycle, the sharp Bragg reflection peaks were recovered and were overlapped with the broad hallow at $2\theta = 20°$ as well as the sharp reflection peaks at $2\theta = 25.5°$ in the low angle region for the S1 and S1′ phases. These low-angle intense reflection peaks were consistent with a layer periodicity of ∼26 Å along the c axis; this was slightly lesser than 29.9897(15) Å, which is obtained based on the single-crystal structural analysis at 100 K after the partial melting of the alkyl chains. The most dominant intermolecular interaction in the molecular assembly of Na^+·**1**·$B(Ph)_4^-$ is the electrostatic cation−anion Coulomb layer in the ab plane, while the hydrophobic $-C_{14}H_{29}$ chains exist in a dynamic state. The melting of the Na^+·**1**·$B(Ph)_4^-$ salt corresponded to the dissociation of the cation−anion pair in the L phase.

3.4. Dielectric Properties. T- and f-dependent dielectric constants are sensitive to the motional freedom of the polar structural unit in a molecular assembly. The real part (ε_1) and imaginary part (ε_2) of the dielectric constants correspond to the capacitance and conductance, respectively. For instance, a typical ionic conductor shows a large ε_2 response due to the contribution of the dielectric-loss. Figure 5a shows the T- and f-dependent ε_1 response and the DSC curve of **1** during the heating cycle. The ε_1-value was 3.2 at 300 K, and it increased to ∼3.5 at the S1−S2 phase transition of solid **1** at 332 K (Figure 5a, inset). This was dominated by a small structural transformation without any drastic change in the motional freedom of the polar structural unit such as N−H···O═ hydrogen-bonding interaction. Further heating of the S2 phase gradually increased the ε_1 values for low-f measurements, and the maximum value of ε_1 ($\varepsilon_1 = 270$) was obtained at T = 355 K and f = 0.316 Hz. Thermal fluctuations of the polar N−H···O═ hydrogen-bonding interactions are activated before the melting of solid **1**, and dissociation of the hydrogen-bonding interaction resulted in melting at the S2−L phase transition. The trend in the ε_2 values was similar to that in the ε_1 values (Figure S11), and the contribution from the ionic conduction was negligible in both S1 and S2 phases. The PXRD patterns of the S2 phase suggested the partial melting of the two $-C_{14}H_{29}$ chains, and it neither affected the dielectric response nor changed the dipole moments.

The ε_1-response of Na^+·**1**·$B(Ph)_4^-$ was remarkably different from that of solid **1**. Figure 5b shows the T- and f-dependent ε_1-response and DSC curves of the Na^+·**1**·$B(Ph)_4^-$ molten salt in the cooling process from 360 K. The Na^+·**1**·$B(Ph)_4^-$ salt showed a complex thermal behavior, accompanied by the formation of the G phase from the L phase during the cooling process. Additionally, two-step crystallization peaks were observed during the heating cycle of the metastable G phase. The ε_1 value for the L to G phase transition at 265 K during the cooling cycle suddenly dropped to 15 after the transition to the G phase. The frozen dipole moments in the G phase were inert for the ε_1-response at 265 K, which was consistent with the DSC measurement. Recrystallization from the metastable G state to the crystalline S1 and S1′ phases in the heating cycle led to the appearance of f-dependent ε_1-peaks around 285 K (Figure S12), suggesting a dynamic structural rearrangement of the polar units in the G phase of Na^+·**1**·$B(Ph)_4^-$. The polar

https://doi.org/10.1021/acs.jpcb.1c03188
J. Phys. Chem. B 2021, 125, 6349−6358

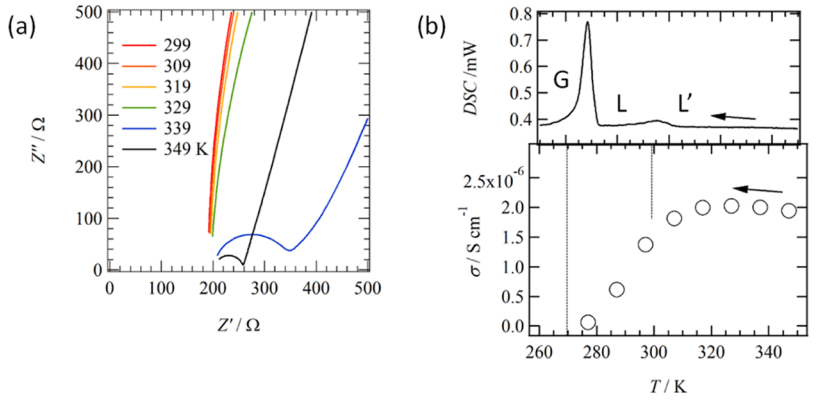

Figure 6. Ionic conduction of the Na^+·**1**·$B(Ph)_4^-$ molten salt in the L phase. (a) *T*-dependent Cole−Cole plots in the *T*-range 299−349 K. (b) DSC curve of the cooling cycle and *T*-dependent σ_{Na} for the G and L phases.

Scheme 2. Phase Transition Behavior and Thermal Cycle of the Na^+·1**·$B(Ph)_4^-$ Salt**[a]

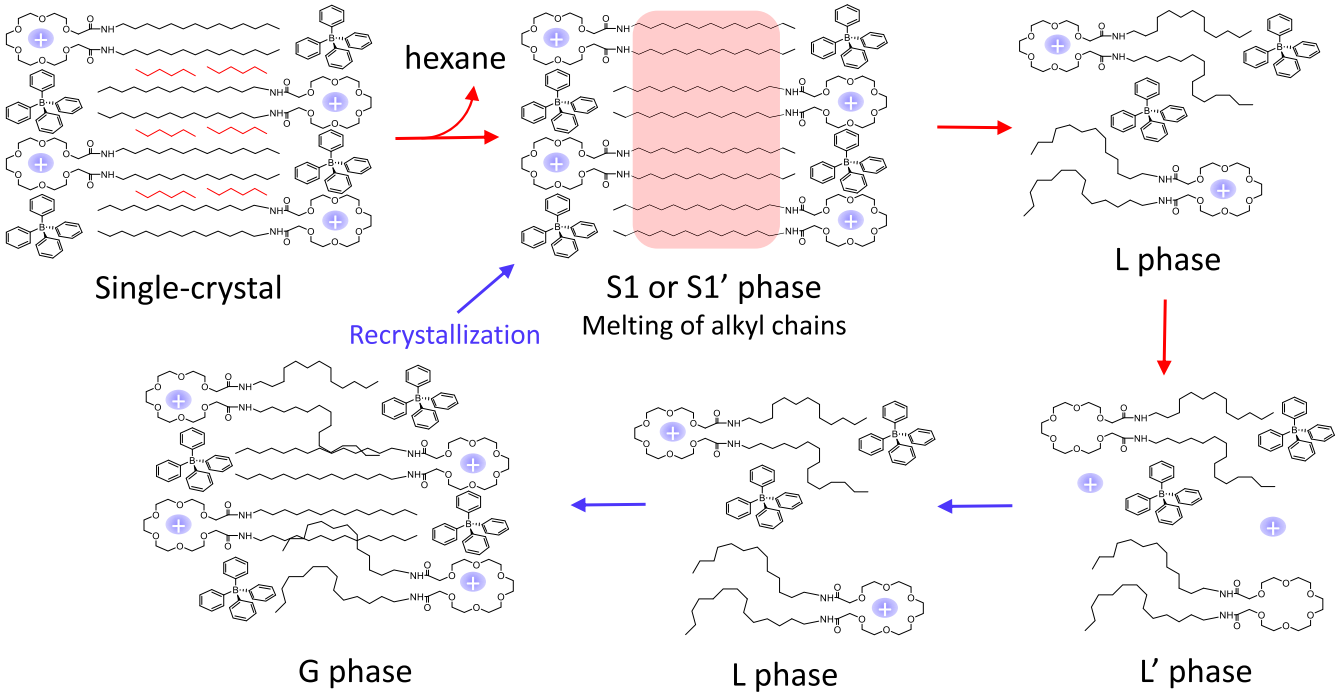

[a]The S1 → S1′ → L → L′ → L → G → S1 cycle was reversibly observed in the Na^+·**1**·$B(Ph)_4^-$ salt.

structural unit in the Na^+·**1**·$B(Ph)_4^-$ molecular assembly is either the N−H···O═ hydrogen-bonding unit or the Na^+−$B(Ph)_4^-$ ion pair. Although the *T*-dependent PXRD patterns of Na^+·**1**·$B(Ph)_4^-$ revealed the existence of the partially melted state of the two long alkyl chains, such dynamics were insensitive to the dielectric spectra. Therefore, reconstruction of the N−H···O═ hydrogen-bonding interaction and cation−anion rearrangement contributed to the recrystallization from the G to S1 (S1′) phase in the heating cycle. This behavior was consistent with the dielectric measurements.

Interestingly, the ε_1 values of the Na^+·**1**·$B(Ph)_4^-$ molten salt in the L phase revealed *T*- and *f*-dependences above 265 K. There are two possible dissociation steps for the cation−anion pairs in the L phase of Na^+·**1**·$B(Ph)_4^-$. The first is the dissociation of Na^+·**1**·$B(Ph)_4^-$ into the Na^+·**1** cationic complex and the $B(Ph)_4^-$ anion, where the Na^+-binding structure of **1** was maintained even in the L phase. The second is the complete dissociation of each component to Na^+, **1**, and $B(Ph)_4^-$, when the Na^+ ions existed freely in the L phase without coordinating to **1**. TG chart of the Na^+·**1**·$B(Ph)_4^-$ molten salt showed the formation of a thermally stable L phase up to 500 K. The ε_1 and ε_2 values of Na^+·**1**·$B(Ph)_4^-$ at 360 K reached 4000 and 6500 at f = 316 Hz, which were two orders of magnitude higher than those of **1** in the L phase. Therefore, the dissociation of the cation−anion pair effectively contributed to the increased dielectric and also to the ionic conductivity of the Na^+·**1**·$B(Ph)_4^-$ molten salt. The DSC curve during cooling from 360 K showed a small endothermic peak at 302 K, with ΔH = 2.70 kJ mol^{-1} (top panel, Figure 6b), where the ε_1 value at low *f* suddenly dropped by two orders of magnitude for the L−G phase transition at 280 K. Therefore, two kinds of liquid phases, L and L′, existed in the Na^+·**1** complex. The latter comprised an independent Na^+ + **1** phase and influenced the dielectric behavior and the Na^+ ionic conductivity of the L phase.

https://doi.org/10.1021/acs.jpcb.1c03188
J. Phys. Chem. B 2021, 125, 6349−6358

The *f*-dependent resistance (Z') and reactance (Z') plots were obtained at different *T*, and the Na^+ conductivity of the Na^+·**1**·$B(Ph)_4^-$ molten salt was determined from the *T*-dependent Cole−Cole ($Z'-Z''$) plots in the cooling cycle from 350 to 299 K (Figure 6a). All the $Z'-Z''$ plots show semicircular traces for typical Na^+ conduction (σ_{Na}, S cm^{-1}); the σ_{Na} value was defined at a cross-sectional point at the horizontal Z'-axis. A stray resistance of ∼200 Ω was observed in all the $Z'-Z''$ plots in the present measurement system. Figure 6b shows the *T*-dependent σ_{Na} value of Na^+·**1**·$B(Ph)_4^-$ in the L phase. The less dynamic Na^+ ions in the G phase decreased the σ_{Na} value to less than 10^{-7} S cm^{-1}, while the G to L phase transition gradually increased the σ_{Na} value up to 2 × 10^{-6} S cm^{-1} at 320 K. The small endothermic peak of the L phase at 302 K in the DSC curve affected the *T*-dependent σ_{Na} value. Thermal activation was observed in the *T*-range 260−300 K, while σ_{Na} was almost *T*-independent in the high-*T* region of the L′ phase above 300 K. Dissociation of the Na^+·**1** complex was observed in the *T*-dependent equilibrium between the Na^+·**1** complex and the completely dissociated independent Na^+ + **1** in the solution phase, indicating the *T*-dependent thermally activated conducting behavior. In contrast, complete dissociation of Na^+ and **1** in the L′ phase corresponded to the *T*-independent behavior of σ_{Na} in the L′ phase.

Single-crystal X-ray structural analysis of Na^+·**1**·$B(Ph)_4^-$·$(hexane)_2$ at 100 K revealed a tight Na^+-binding structure of **1** held by intramolecular N−H···O= hydrogen-bonding interactions, which can be used to explain the phase transition behavior of Na^+·**1**·$B(Ph)_4^-$. First, the elimination of the crystallized hexane molecules at 298 K resulted in the formation of the crystalline S1 phase, in which the two alkyl chains had motional freedom with a partially melted state and the electrostatic cation−anion Coulomb layer was effectively maintained (Scheme 2). Heating of the S1 and S1′ phases resulted in the transition to the molten L phase, in which the Na^+ cation was still tightly bounded by **1** to form the Na^+·**1** complex as the counter cation of bulky $B(Ph)_4^-$. Further heating of the L phase changed the molecular assembly of the Na^+·**1** complex to free Na^+ + **1** species in the L′ phase. Cooling of this phase reconstructed the L phase to form the Na^+·**1** complex and $B(Ph)_4^-$ anion. Further cooling of the L phase fixed the random orientation of each cation−anion pair with a disordered conformation of the alkyl chains, forming the G phase. The metastable G phase was transformed into the stable crystalline S1 and S1′ phases upon heating, and the thermal energy modulated the cation−anion Coulomb pair to recover the 2D electrostatic lattice as well as the partially melted conformation of the two $-C_{14}H_{29}$ chains. The S1 → S1′ → L → L′ → L → G → S1 thermal cycle was reversibly observed in heating and cooling cycles of the Na^+·1·$B(Ph)_4^-$ salt.

4. CONCLUSIONS

A penta(ethylene glycol) derivative (**1**) bearing two hydrogen-bonding $-CONHC_{14}H_{29}$ chains was prepared to achieve both ion-recognition and hydrogen-bonding abilities. Compound **1** exhibited a much higher Na^+-binding ability than K^+-binding ability in the solution phase, which was consistent with the molecular structure of the Na^+·**1** complex based on the single crystal X-ray structural analysis at 100 K. The six ether oxygen atoms of penta(ethylene glycol) and one carbonyl O= oxygen atom at the −CONH− site were tightly coordinated to the Na^+ ion in a wrapped conformation, which was further stabilized by the intramolecular N−H···O= hydrogen-bonding interaction and hydrophobic interactions between the two long $-C_{14}H_{29}$ alkyl chains. Although the structural unit of **1**, which contains six ether oxygen atoms, is the same as that of [18]crown-6, the Na^+-binding ability of the acyclic compound **1** was higher than that of cyclic [18]crown-6. The multiple Na^+···O interactions effectively trapped the Na^+ cation inside the hydrophilic penta(ethylene glycol) unit. The two hydrophobic alkyl chains interacted via multiple van der Waals forces, supporting the Na^+-bound conformation. The electrostatic cation−anion layer and hydrophobic alkyl chains formed a 2D lamella-like molecular assembly. Thermal analysis of solid **1** revealed the existence of an S1−S2 phase transition while that of the Na^+·**1**·$B(Ph)_4^-$ salt showed a complex phase transition sequence, L → G → S1 → S1′ → L → L′ → L → G → S1. The ionic conductivity of Na^+ in the Na^+·**1**·$B(Ph)_4^-$ molten salt in the L phase showed two kinds of dynamics in the *T*- and *f*-dependent dielectric responses. The σ_{Na} values in the L phase were dominated by thermal activation in an equilibrium between the Na^+·**1** complex and dissociated species of Na^+ + **1**, while the complete dissociation of Na^+ and **1** in the L′ phase showed a *T*-independent conducting behavior. Thermally activated molecular motion of the electrostatic cation−anion Coulomb pairs and the melting state of the alkyl chains were randomly fixed in the G phase, which was reconstructed in the stable crystalline phase during the heating cycle. The electrostatic cation−anion Coulomb interaction first reappeared, and the alkyl chains regained their conformation to the lamella-type molecular assembly. The conformational freedom and ion-recognition ability of the acyclic amphiphilic **1** render it a potential compound in the fabrication of ion-sensing and ionic channel materials. After harnessing other physical properties such as electrical conduction and fluorescent responses, such materials can be used to construct multifunctional molecular assemblies.

■ ASSOCIATED CONTENT

Supporting Information

The Supporting Information is available free of charge at https://pubs.acs.org/doi/10.1021/acs.jpcb.1c03188.

IR spectra; NMR spectra of **1** and the change in Na^+ and K^+ addition; TG charts;, POM images of **1** and Na^+·**1**·$B(Ph)_4^-$; single-crystal X-ray structural analyses; simulated PXRD patterns; *T*- and *f*-dependent imaginary part dielectric constants; and *T*- and *f*-dependent dielectric constants of G−S1 (S1′) transitions (PDF)

■ AUTHOR INFORMATION

Corresponding Author

Tomoyuki Akutagawa − *Graduate School of Engineering, Tohoku University, Sendai 980-8579, Japan; Institute of Multidisciplinary Research for Advanced Materials (IMRAM), Tohoku University, Sendai 980-8577, Japan;* orcid.org/0000-0003-3040-1078; Phone: +81-22-217-5653; Email: akutagawa@tohoku.ac.jp; Fax: +81-22-217-5655

Authors

Shinya Seto − *Graduate School of Engineering, Tohoku University, Sendai 980-8579, Japan*

Takashi Takeda − *Graduate School of Engineering, Tohoku University, Sendai 980-8579, Japan; Institute of*

https://doi.org/10.1021/acs.jpcb.1c03188
J. Phys. Chem. B 2021, 125, 6349−6358

Multidisciplinary Research for Advanced Materials (IMRAM), Tohoku University, Sendai 980-8577, Japan; orcid.org/0000-0002-5254-2819

Norihisa Hoshino − *Graduate School of Engineering, Tohoku University, Sendai 980-8579, Japan; Institute of Multidisciplinary Research for Advanced Materials (IMRAM), Tohoku University, Sendai 980-8577, Japan;* orcid.org/0000-0002-9841-6375

Complete contact information is available at: https://pubs.acs.org/10.1021/acs.jpcb.1c03188

Notes

The authors declare no competing financial interest.

■ ACKNOWLEDGMENTS

This work was supported by a Grant-in-Aid for Scientific Research on KAKENHI (JP19H00886, JP20H05865, JP20K05442, and JP20H04655), JST CREST (grant number JPMJCR18I4), and the "Dynamic Alliance for Open Innovation Bridging Human, Environment and Materials" project supported by MEXT.

■ REFERENCES

(1) Pedersen, C. J. Cyclic polyethers and their complexes with metal salts. *J. Am. Chem. Soc.* **1967**, *89*, 7017−7036.
(2) Liu, Z.; Nalluri, S. K. M.; Stoddart, J. F. Surveying macrocyclic chemistry: From flexible crown ethers to rigid cyclophanes. *Chem. Soc. Rev.* **2017**, *46*, 2459−2478.
(3) *Crown Ethers and Analogs*; Patai, S., Rappoport, Z., Eds.; John Wiley & Sons, 1989.
(4) Gokel, G. W.; Leevy, W. M.; Weber, M. E. Crown ethers: Sensors for ions and molecular scaffolds for materials and biological models. *Chem. Rev.* **2004**, *104*, 2723−2750.
(5) Buchanan, G. W.; Gerzain, M.; Bensimon, C. 1,4,7,10,13-Pentaoxacyclopentadecane (15-crown-5) sodium iodide complex, $C_{10}H_{20}O_5$•NaI. *Acta Crystallogr., Sect. C: Cryst. Struct. Commun.* **1994**, *50*, 1016−1019.
(6) Dunitz, J. D.; Dobler, M.; Seiler, P.; Phizackerley, R. P. Crystal structure analyses of 1,4,7,10,13,16-hexaoxacyclooctadecane and its complexes with alkali thiocyanates. *Acta Crystallogr., Sect. B: Struct. Crystallogr. Cryst. Chem.* **1974**, *30*, 2733−2738.
(7) Thompson, M. A.; Glendening, E. D.; Feller, D. The nature of K^+/crown ether interactions: A hybrid quantum mechanical-molecular mechanical study. *J. Phys. Chem.* **1994**, *98*, 10465−10476.
(8) Bruning, H.; Feil, D. Electrostatic interactions in host-guest complexes 2. *J. Comput. Chem.* **1991**, *12*, 1−8.
(9) Izatt, R. M.; Bradshaw, J. S.; Nielsen, S. A.; Lamb, J. D.; Christensen, J. J.; Sen, D. Thermodynamic and kinetic data for cation-macrocycle interaction. *Chem. Rev.* **1985**, *85*, 271−339.
(10) Izatt, R. M.; Pawlak, K.; Bradshaw, J. S.; Bruening, R. L. Thermodynamic and kinetic data for macrocycle interaction with cations, anions, and neutral molecules. *Chem. Rev.* **1995**, *95*, 2529−2586.
(11) Chan, K. W. S.; Cook, K. D. Mass spectrometric study of interactions between poly(ethylene glycols) and alkali metals in solution. *Macromolecules* **1983**, *16*, 1736−1740.
(12) Poudel, L.; Podgornik, R.; Ching, W.-Y. The hydration effect and selectivity of alkali metal ions on poly(ethylene glycol) models in cyclic and linear topology. *J. Phys. Chem. A* **2017**, *121*, 4721−4731.
(13) Breton, M. F.; Discala, F.; Bacri, L.; Foster, D.; Pelta, J.; Oukhaled, A. Exploration of neutral versus polyelectrolyte behavior of poly(ethylene glycol)s in alkali ion solutions using single-nanopore recording. *J. Phys. Chem. Lett.* **2013**, *4*, 2202−2208.
(14) Frensdorff, H. K. Stability constants of cyclic polyether complexes with univalent cations. *J. Am. Chem. Soc.* **1971**, *93*, 600−606.
(15) Haymore, B. L.; Lamb, J. D.; Izatt, R. M.; Christensen, J. J. Thermodynamic origin of the macrocyclic effect in crown ether complexes of sodium(1+), potassium(1+), and barium(2+). *Inorg. Chem.* **1982**, *21*, 1598−1602.
(16) Zhang, H.; Dearden, D. V. The gas-phase macrocyclic effect: Reaction rates for crown ethers and the corresponding glymes with alkali metal cations. *J. Am. Chem. Soc.* **1992**, *114*, 2754−2755.
(17) Akutagawa, T. Dynamic molecular assemblies toward a new frontier in materials chemistry. *Mater. Chem. Front.* **2018**, *2*, 1064−1073.
(18) Akutagawa, T. Chemical design and physical properties of dynamic molecular assemblies. *Bull. Chem. Soc. Jpn.* **2021**, *94*, 1400−1420.
(19) Han, Y.; Meng, Z.; Ma, Y.-X.; Chen, C.-F. Iptycene-derived crown ether hosts for molecular recognition and self-assembly. *Acc. Chem. Res.* **2014**, *47*, 2026−2040.
(20) Fu, D.-W.; Zhang, W.; Cai, H.-L.; Zhang, Y.; Ge, J.-Z.; Xiong, R.-G.; Huang, S. D. Supramolecular bola-like ferroelectric: 4-methoxyanilinium tetrafluoroborate-18-crown-6. *J. Am. Chem. Soc.* **2011**, *133*, 12780−12786.
(21) Tang, Y.-Z.; Yu, Y.-M.; Xiong, J.-B.; Tan, Y.-H.; Wen, H.-R. Unusual High-Temperature Reversible Phase-Transition Behavior, Structures, and Dielectric-Ferroelectric Properties of Two New Crown Ether Clathrates. *J. Am. Chem. Soc.* **2015**, *137*, 13345−13351.
(22) Ye, H.-Y.; Zhang, Y.; Fu, D.-W.; Xiong, R.-G. A displacive-type metal crown ether ferroelectric compound: $Ca(NO_3)_2$(15-crown-5). *Angew. Chem., Int. Ed.* **2014**, *53*, 6724−6729.
(23) Akutagawa, T.; Koshinaka, H.; Sato, D.; Takeda, S.; Noro, S.-i.; Takahashi, H.; Kumai, R.; Tokura, Y.; Nakamura, T. Ferroelectricity and polarity control in solid-state flip-flop supramolecular rotators. *Nat. Mater.* **2009**, *8*, 342−347.
(24) Hayata, A.; Itoh, H.; Inoue, M. Solid-phase total synthesis and dual mechanism of action of the channel-forming 48-mer peptide polytheonamide B. *J. Am. Chem. Soc.* **2018**, *140*, 10602−10611.
(25) Muraoka, T.; Noguchi, D.; Kasai, R. S.; Sato, K.; Sasaki, R.; Tabata, K. V.; Ekimoto, T.; Ikeguchi, M.; Kamagata, K.; Hoshino, N.; Noji, H.; Akutagawa, T.; Ichimura, K.; Kinbara, K. A synthetic ion channel with anisotropic ligand response. *Nat. Commun.* **2020**, *11*, 2924.
(26) Eisenberg, B. Ionic channels in biological membranes: Natural nanotubes. *Acc. Chem. Res.* **1998**, *31*, 117−123.
(27) Schneider, S.; Licsandru, E.-D.; Kocsis, I.; Gilles, A.; Dumitru, F.; Moulin, E.; Tan, J.; Lehn, J.-M.; Giuseppone, N.; Barboiu, M. Columnar self-assemblies of triarylamines as scaffolds for artificial biomimetic channels for ion and for water transport. *J. Am. Chem. Soc.* **2017**, *139*, 3721−3727.
(28) Nakamura, T.; Akutagawa, T.; Honda, K.; Underhill, A. E.; Coomber, A. T.; Friend, R. H. A molecular metal with ion-conducting channels. *Nature* **1998**, *394*, 159−162.
(29) Akutagawa, T.; Hasegawa, T.; Nakamura, T.; Takeda, S.; Inabe, T.; Sugiura, K.-i.; Sakata, Y.; Underhill, A. E. Ionic channel structures in $(M^+)_x$(18-crown-6)$[Ni(dmit)_2]_2$ molecular conductors, Chem. *Chem.—Eur. J.* **2001**, *7*, 4902−4912.
(30) Akutagawa, T.; Hasegawa, T.; Nakamura, T.; Inabe, T. Supramolecular cation assemblies of hydrogen-bonded (NH_4^+/$NH_2NH_3^+$)(crown ether) in $[Ni(dmit)_2]^-$ based molecular conductors and magnets. *J. Am. Chem. Soc.* **2002**, *124*, 8903−8911.
(31) Akutagawa, T.; Hasegawa, T.; Nakamura, T.; Sugiura, K.-i.; Sakata, Y.; Inabe, T.; Underhill, A. E. Supramolecular cation of an acyclic polyether: Potassium(pentaethylene glycol) in a molecular conducting nickel dithiolate salt. *Chem. Commun.* **1998**, 2599−2600.
(32) Mindemark, J.; Lacey, M. J.; Bowden, T.; Brandell, D. Beyond PEO − Alternative host materials for Li^+-conducting solid polymer electrolytes. *Prog. Polym. Sci.* **2018**, *81*, 114−143.
(33) *Polymer Electrolyte*; Gray, F. M., Connor, J. A., Eds.; RSC: Cambridge, 1997.
(34) Won, Y.-Y.; Brannan, A. K.; Davis, H. T.; Bates, F. S. Cryogenic transmission electron microscopy (cryo-TEM) of micelles and

vesicles formed in water by poly(ethylene oxide)-based block copolymers. *J. Phys. Chem. B* **2002**, *106*, 3354−3364.
(35) Sou, K.; Endo, T.; Takeoka, S.; Tsuchida, E. Poly(ethylene glycol)-modification of the phospholipid vesicles by using the spontaneous incorporation of poly(ethylene glycol)-lipid into the vesicles. *Bioconjugate Chem.* **2000**, *11*, 372−379.
(36) Knop, K.; Hoogenboom, R.; Fischer, D.; Schubert, U. S. Poly(ethylene glycol) in drug delivery: Pros and cons as well as potential alternatives. *Angew. Chem., Int. Ed.* **2010**, *49*, 6288−6308.
(37) Alcantar, N. A.; Aydil, E. S.; Israelachvili, J. N. Polyethylene glycol-coated biocompatible surfaces. *J. Biomed. Mater. Res.* **2000**, *51*, 343−351.
(38) Shimizu, T.; Masuda, M.; Minamikawa, H. Supramolecular nanotube architectures based on amphiphilic molecules. *Chem. Rev.* **2005**, *105*, 1401−1444.
(39) Petty, M. C. *Langmuir-Blodgett Films: An Introduction*; Cambridge University Press, 1996.
(40) Ramanathan, M.; Shrestha, L. K.; Mori, T.; Ji, Q.; Hill, J. P.; Ariga, K. Amphiphile nanoarchitectonics: From basic physical chemistry to advanced applications. *Phys. Chem. Chem. Phys.* **2013**, *15*, 10580−10611.
(41) Rumble, K. *CRC Handbook of Chemistry and Physics*, 100th ed.; CRC Press, 2019.
(42) Imaeda, K.; Enoki, T.; Shi, Z.; Wu, P.; Okada, N.; Yamochi, H.; Saito, G.; Inokuchi, H. Electrical Conductivities of Tetrakis-(alkylthio)tetrathiafulvalene (TTCn-TTF) and Tetrakis(alkyltelluro)-tetrathiafulvalene (TTeCn-TTF). *Bull. Chem. Soc. Jpn.* **1987**, *60*, 3163−3167.
(43) Ukai, S.; Igarashi, S.; Nakajima, M.; Marumoto, K.; Ito, H.; Kuroda, S.; Nishimura, K.; Enomoto, Y.; Saito, G. Molecular-fastener effects on transport property of TTCn-TTF field-effect transistors. *Colloids Surf., A* **2006**, *284*−*285*, 589−593.
(44) Ungar, G.; Masic, N. Order in the rotator phase of n-alkanes. *J. Phys. Chem.* **1985**, *89*, 1036−1042.
(45) Cholakova, D.; Denkov, N. Rotator phases in alkane systems: In bulk, surface layers and micro/nano-confinements. *Adv. Colloid Interface Sci.* **2019**, *269*, 7−42.
(46) Collings, P. J.; Hird, M.. In *Introduction to Liquid Crystals, Chemistry and Physics*; Gray, G. W., Goodby, J. W., Fukuda, A., Eds.; Taylor & Francis: London, 1997.
(47) Chandrasekhar, S. *Liquid Crystal*; Cambridge University Press: Newyork, 1992.
(48) Kobayashi, Y.; Matsunaga, Y. New Discogenic Compounds:N,N′-Dialkanoyl-2,3,5,6-tetrakis(alkanoyloxy)-1,4-benzenediamines. *Bull. Chem. Soc. Jpn.* **1987**, *60*, 3515−3518.
(49) Matsunaga, Y.; Miyajima, N.; Nakayasu, Y.; Sakai, S.; Yonenaga, M. Design of Novel Mesomorphic Compounds:N,N′,N″-Trialkyl-1,3,5-benzenetricarboxamides. *Bull. Chem. Soc. Jpn.* **1988**, *61*, 207−210.
(50) Matsunaga, Y.; Nakayasu, Y.; Sakai, S.; Yonenaga, M. Liquid Crystal Phases Exhibited by N,N′,N″-Trialkyl-1,3,5-Benzenetricaboxamides. *Mol. Cryst. Liq. Cryst.* **2011**, *141*, 327−333.
(51) Fitié, C. F. C.; Roelofs, W. S. C.; Kemerink, M.; Sijbesma, R. P. Remnant polarization in thin films from a columnar liquid crystal. *J. Am. Chem. Soc.* **2010**, *132*, 6892−6893.
(52) Fitié, C. F. C.; Roelofs, W. S. C.; Magusin, P. C. M. M.; Wübbenhorst, M.; Kemerink, M.; Sijbesma, R. P. Polar switching in trialkylbenzene-1,3,5-tricarboxamides. *J. Phys. Chem. B* **2012**, *116*, 3928−3937.
(53) Urbanaviciute, I.; Meng, X.; Cornelissen, T. D.; Gorbunov, A. V.; Bhattacharjee, S.; Sijbesma, R. P.; Kemerink, M. Tuning the ferroelectric properties of trialkylbenzene-1,3,5-tricarboxamide (BTA). *Adv. Electron. Mater.* **2017**, *3*, 1600530.
(54) Wu, J.; Takeda, T.; Hoshino, N.; Akutagawa, T. Ferroelectric low-voltage ON/OFF switching of chiral benzene-1,3,5-tricarboxamide derivative. *J. Mater. Chem. C* **2020**, *8*, 10283−10289.
(55) Shishido, Y.; Anetai, H.; Takeda, T.; Hoshino, N.; Noro, S.-i.; Nakamura, T.; Akutagawa, T. Molecular assembly and ferroelectric response of benzenecarboxamides bearing multiple $-CONHC_{14}H_{29}$ chains. *J. Phys. Chem. C* **2014**, *118*, 21204−21214.
(56) Anetai, H.; Wada, Y.; Takeda, T.; Hoshino, N.; Yamamoto, S.; Mitsuishi, M.; Takenobu, T.; Akutagawa, T. Fluorescent ferroelectrics of hydrogen-bonded pyrene derivatives. *J. Phys. Chem. Lett.* **2015**, *6*, 1813−1818.
(57) Anetai, H.; Takeda, T.; Hoshino, N.; Araki, Y.; Wada, T.; Yamamoto, S.; Mitsuishi, M.; Tsuchida, H.; Ogoshi, T.; Akutagawa, T. Circular polarized luminescence of hydrogen-bonded molecular assemblies of chiral pyrene derivatives. *J. Phys. Chem. C* **2018**, *122*, 6323−6331.
(58) Anetai, H.; Sambe, K.; Takeda, T.; Hoshino, N.; Akutagawa, T. Nanoscale effects in one-dimensional columnar supramolecular ferroelectrics. *Chem.—Eur. J.* **2019**, *25*, 11233−11239.
(59) Wu, J.; Takeda, T.; Hoshino, N.; Suzuki, Y.; Kawamata, J.; Akutagawa, T. Ferroelectricity of a tetraphenyl porphyrin derivative bearing $-CONHC_{14}H_{29}$ chains at 500 K. *J. Phys. Chem. C* **2019**, *123*, 22439−22446.
(60) Anetai, H.; Takeda, T.; Hoshino, N.; Kobayashi, H.; Saito, N.; Shigeno, M.; Yamaguchi, M.; Akutagawa, T. Ferroelectric alkylamide-substituted helicene derivative with two-dimensional hydrogen-bonding lamellar phase. *J. Am. Chem. Soc.* **2019**, *141*, 2391−2397.
(61) *Crystal Structure: Single Crystal Structure Analysis Software*, Ver. 3.6; Rigaku Corporation and Molecular Structure Corporation, 2004.
(62) Sheldrick, G. M. *SHELX Programs for Crystal Structure Analysis*; Universität Göttingen: Göttingen, Germany, 2018.

https://doi.org/10.1021/acs.jpcb.1c03188
J. Phys. Chem. B 2021, 125, 6349−6358